Astronomy & Astrophysics Vol. 690, A321, 14
October 21, 2024

Revealing faint compact radio jets at redshifts above 5 with very long baseline interferometry

M. Krezinger[1,2,3,⋆], G. Baldini[4], M. Giroletti[5], T. Sbarrato[6], G. Ghisellini[6], G. Giovannini[4,5], T. An[7], K. É. Gabányi[1,9,2,3], S. Frey[2,3,8]

[1] Department of Astronomy, Institute of Physics and Astronomy, ELTE Eötvös Loránd University, Pázmány Péter sétány 1/A, H-1117 Budapest, Hungary
[2] Konkoly Observatory, HUN-REN Research Centre for Astronomy and Earth Sciences, Konkoly Thege Miklós út 15-17, H-1121 Budapest, Hungary
[3] CSFK, MTA Centre of Excellence, Konkoly Thege Miklós út 15-17, H-1121 Budapest, Hungary
[4] Dipartimento di Fisica e Astronomia, Università di Bologna, Via P. Gobetti 93/2, 40129 Bologna, Italy
[5] INAF Istituto di Radioastronomia, via Gobetti 101, 40129, Bologna, Italy
[6] INAF Osservatorio Astronomico di Brera, Via E. Bianchi 46, 23807, Merate, Italy
[7] Shanghai Astronomical Observatory, Key Laboratory of Radio Astronomy and Technology, Chinese Academy of Sciences, 80 Nandan Road, Shanghai 200030, China
[8] Institute of Physics and Astronomy, ELTE Eötvös Loránd University, Pázmány Péter sétány 1/A, H-1117 Budapest, Hungary
[9] HUN-REN–ELTE Extragalactic Astrophysics Research Group, Eötvös Loránd University, Pázmány Péter sétány 1/A, H-1117 Budapest, Hungary

Received 7 June 2024 / Accepted 21 July 2024

ABSTRACT

Context. Over the past two decades, our knowledge of the high-redshift ($z > 5$) radio quasars has expanded, thanks to dedicated high-resolution very long baseline interferometry (VLBI) observations. Distant quasars provide unique information about the formation and evolution of the first galaxies and supermassive black holes in the Universe. Powerful relativistic jets are likely to have played an essential role in these processes. However, the sample of VLBI-observed radio quasars is still too small to allow meaningful statistical conclusions.

Aims. We extend the list of the VLBI observed radio quasars to investigate how the source structure and physical parameters are related to radio loudness.

Methods. We assembled a sample of ten faint radio quasars located at $5 < z < 6$ with their radio-loudness indices spanning between $0.9 - 76$. We observed the selected targets with the European VLBI Network (EVN) at 1.7 GHz. The milliarcsecond-scale resolution of VLBI at this frequency allowed us to probe the compact innermost parts of radio-emitting relativistic jets. In addition to the single-band VLBI observations, we collected single-dish and low-resolution radio interferometric data to investigate the spectral properties and variability of our sources.

Results. The detection rate of this high-redshift, low-flux-density sample is 90%, with only one target (J0306+1853) remaining undetected. The other nine sources appear core-dominated and show a single, faint and compact radio core on this angular scale. The derived radio powers are typical of Fanaroff-Riley II radio galaxies and quasars. By extending our sample with other VLBI-detected $z > 5$ sources from the literature, we found that the core brightness temperatures and monochromatic radio powers tend to increase with radio loudness.

Key words. radio continuum: galaxies — galaxies: active — galaxies: high-redshift — galaxies: jets

1. Introduction

There are currently several hundred quasars known at redshift $z > 5$ and their number is increasing (e.g. Fan et al. 1999; Bañados et al. 2016; Jiang et al. 2016; Wang et al. 2019; Onken et al. 2022; DESI Collaboration et al. 2024; Yue et al. 2023). Their studies provide essential information about how galaxies formed and evolved in the early Universe. Quasars can be divided into two populations based on their radio-loudness parameter, i.e. the radio-to-optical power ratio usually expressed as $R_{4400\,\text{Å}} = L_{5\,\text{GHz}}/L_{4400\,\text{Å}}$ (Kellermann et al. 1989, 2016) or $R_{2500\,\text{Å}} = L_{5\,\text{GHz}}/L_{2500\,\text{Å}}$ (Sramek & Weedman 1980). Radio-loud quasars (RLQs) are defined with $R > 10$ and they represent only $\sim 10\%$ of the known quasars (e.g. Begelman et al. 1984; Ivezić et al. 2002), also at high redshifts (Bañados et al. 2015). Their radio emission originates mainly from powerful relativistic plasma jets (e.g. Padovani et al. 2015; Blandford et al. 2019). On the other hand, the nature of the the emission of radio-quiet quasars (RQQs, $R \leq 10$) is less obvious. RQQs make up the majority of the active galactic nuclei (AGN) population at every redshift, therefore their study is crucial for understanding the nature of AGN in general. They are thought not to host high-power jets. Their radio emission generally originates from star-forming activity in their host galaxy, accretion disk winds, coronal emission, or shock regions due to the interaction between the outflows and interstellar clouds (Panessa et al. 2019). These mechanisms operate at different spatial scales and radio frequencies. Recently, Sbarrato et al. (2021) revealed that at high redshifts,

⋆ E-mail: krezinger.mate@csfk.org

some massive ($M > 10^{10}\,M_\odot$) RQQs host powerful relativistic jets, which seems to be at odds with the above model.

The distant AGN are known to host supermassive black holes (SMBHs) with $M_{BH} > 3\times10^8\,M_\odot$, with the majority being more massive than $10^9\,M_\odot$ (e.g. Wang et al. 2013; Shen et al. 2019; Sbarrato 2021). Detecting preferentially these objects is clearly a selection bias, as they are the most powerful sources of radiation, easily observable even from vast distances corresponding to high redshifts. The presence of $M_{BH} \gtrsim 10^{8-9}\,M_\odot$ black holes raises important questions about the formation and evolution of the first SMBHs in the Universe. Volonteri (2012) and Inayoshi et al. (2020) reviewed the possible mechanisms to build up SMBHs in excess of $10^9\,M_\odot$ in less than 1 Gyr. It can only be achieved via fast accretion in a super-Eddington regime, or assuming black hole seeds of $\sim 10^4\,M_\odot$ as a starting point not to violate the Eddington limit. Jets might play an important role in assembling such massive early black holes. This can be explained by a simple model (e.g. Ghisellini et al. 2013; Sbarrato 2021; Sbarrato et al. 2022) where the relativistic jets carry away some of the released gravitational energy, allow for a faster accretion at the same observed luminosity. The distribution of jets in the early Universe, whether they are connected to RLQs or RQQs, is important to understand their link to the formation of the first SMBHs.

Another intriguing observational result regarding the high-redshift AGN, inferred by the presence of blazars (i.e. sources with their jets aligned close to the line of sight, $\theta \lesssim 10°$), is that the fraction of the most massive ($> 10^9\,M_\odot$) black holes hosted in radio-loud (jetted) AGN is larger than those found in RQQs at $z > 4$ compared to more recent cosmological epochs (Ghisellini et al. 2013; Sbarrato et al. 2015; Sbarrato 2021). It appears that high-redshift AGN with the most massive black holes prefer to have relativistic jets. There are a few scenarios that can explain the problem of missing RQQs. Volonteri et al. (2011) proposed the idea that the difference might be due to internal and external absorption mechanisms in AGN, or lower bulk Lorentz factors in jets in the early Universe. It is also possible that the current survey sensitivity causes bias. At high redshift, Ghisellini et al. (2015a) found the radio lobes dimmed due to the interaction of their electrons with photons of the cosmic microwave background. The early galaxies may also be obscured by a dense dust bubble surrounding the central region of the AGN (Ghisellini & Sbarrato 2016) and only the most powerful jets are able to penetrate this bubble, sweeping away most of the material along their path. The absence of direct link between radio-loudness and jet presence raises the question whether there is a missing population of relativistic jets hosted in RQQs. Or we are simply misclassifying a fraction of blazar candidates based on X-ray and low-resolution radio observations (e.g. Cao et al. 2017; Coppejans et al. 2016; Krezinger et al. 2022).

To reliably observe jets in RQQs, parsec-scale resolution is required, because the radio emission on this scale is closely associated with the central engine. On the other hand, low-resolution observations (arcsecond-scale) trace the total radio flux density, a composite emission of the different mechanisms, which cannot be directly linked to the optical, X-ray, or infrared emissions coming from the AGN. However, low-resolution interferometric surveys are the starting point for any follow-up radio jet study. The Faint Images of the Radio Sky at Twenty-Centimeters (FIRST, White et al. 1997) survey catalogue at 1.4-GHz and the recent, still ongoing multi-epoch Very Large Array Sky Survey (VLASS, Lacy et al. 2020; Gordon et al. 2020, 2021) provide essential spectral and structural information in help to select targets for high-resolution observations. The technique of very long baseline interferometry (VLBI) can achieve parsec-scale linear resolution at cm wavelengths and is capable to distinguish between compact emission with high brightness temperature and a more extended radio feature. Only a few dozens of RQQs have been observed with VLBI (Blundell & Beasley 1998; Middelberg et al. 2004; Ulvestad et al. 2005; Giroletti & Panessa 2009; Panessa & Giroletti 2013; Herrera Ruiz et al. 2016; Krezinger et al. 2020; Wang et al. 2023a), and very few that can be found at high redshift (i.e. $z > 4$, Klöckner et al. 2009; Sbarrato et al. 2021).

VLBI can provide useful astrometric information as well. Phase-referenced VLBI observations (Beasley & Conway 1995), where nearby calibrator sources provide relative astrometric positions for the targeted radio-emitting features, can be accurate to milliarcsecond (mas) level. This accuracy is comparable to the precise optical astrometric data from the recent 3rd Data Release (DR3) of the *Gaia* mission (Gaia Collaboration et al. 2016, 2023). The optical position, if available, in addition to the VLBI radio position, adds further relevant astrophysical and morphological information about the source. The optical position marks the location of the AGN accretion disk or, in some cases, its blend with the optical synchrotron emission of the innermost sub-milliarcsecond scale jet (Plavin et al. 2019). Unlike the optical, the VLBI intensity peak pinpoints the brightest and most compact emission feature, the self-absorbed base of the jet (i.e. the core), or sometimes a shock front (i.e. a hotspot in a lobe) in an extended radio source (Kovalev et al. 2017).

In this paper, we present VLBI observations of ten $z > 5$ radio quasars with different radio-loudness indices. This way, we expect to cover a variety of radio-emitting AGN in order to understand whether the radio-loudness cut is meaningful in terms of the presence of relativistic jets at such high redshifts. The experiment was carried out with the European VLBI Network (EVN) combined with e-MERLIN (Enhanced Multi-Element Radio-Linked Interferometer Network) antennas at the frequency of 1.7 GHz in 2022. The sensitivity and high angular resolution of the EVN allow us to detect compact core–jet features. With the inclusion of e-MERLIN stations, it is also possible to detect extended ($\sim 0\farcs1$) emission if present. The goal was to investigate the nature of these sources using high-resolution VLBI imaging data, together with radio spectral information found in the literature, and the recent *Gaia* DR3 optical positions where available. By involving literature data about other known $z > 5$ quasars as well, we investigate how the milliarcsecond-scale properties are related to the radio loudness of the sources.

In Section 2, we introduce the sample of ten objects targeted with the EVN. In Section 3, the details of the observations and data reduction are provided. Our result are given in Section 4 and discussed in Section 5. The findings of this study are summarised in Section 6. Throughout this paper, we assume a standard flat Λ Cold Dark Matter cosmological model with $\Omega_m = 0.3$, $\Omega_\Lambda = 0.7$, and $H_0 = 70\ \mathrm{km\,s^{-1}\,Mpc^{-1}}$, and used these parameters in the cosmology calculator of Wright (2006). In this model, the typical linear scale is $\sim 6\ \mathrm{pc\,mas^{-1}}$ and the luminosity distance of our sources is ~ 50 Gpc.

2. Target sample

With this study, we aim to extend the list of the VLBI-observed high-redshift radio-quiet quasars. To this end, we searched for faint radio emitters among the sources in the catalogue of the known $z > 5$ quasars compiled by Ross & Cross (2020). From this catalogue, the nine sources with the lowest radio power were selected. These have VLASS detection but have not been ob-

served with VLBI yet. Their 2.7-GHz VLASS flux densities are ranging between 1 mJy $< S_{2.7\,\mathrm{GHz}} <$ 11 mJy. Six of them were also detected in the 1.4-GHz FIRST survey. The 10th target, SDSS J0306+1853, having one of the most massive known SMBHs among quasars at $z > 5$ with $1.1{\times}10^{10}$ $M_\odot$ (Wang et al. 2015), is also included in the sample. It was previously investigated by Sbarrato et al. (2021) and found to be unresolved on arcsecond scales with the *Karl G. Jansky* Very Large Array (JVLA), suggesting the presence of a compact radio jet. Its flux densities were 0.25 mJy and 0.09 mJy at 1.5 and 5 GHz frequencies, respectively (Sbarrato et al. 2021). There were no other radio observations of this quasar.

Table 1 contains the parameters of the selected radio sources. Since all but one of them have VLASS detection, for the sake of simplicity and uniformity, we calculated the radio loudness index using the 2.7-GHz flux density as $R = L_{2.7\,\mathrm{GHz}}/L_{4400\,\mathrm{A}}$. In the case of J0306+1853 which is not detected in VLASS, we used the flux densities and spectral index derived by Sbarrato et al. (2021) to estimate the 2.7-GHz radio power. The 10 sources in our sample have radio loudness in the range $0.9 \leq R \leq 76$.

3. Observations and data reduction

3.1. EVN observations

The selected ten faint radio sources were observed with the EVN at a single frequency band centred around 1.66 GHz. The observations were carried out in two sessions under the project code EG119 (PI: G. Baldini), one with nine targets in 2022 June 3 (EG119A) and another with J0306+1853 as the only target in 2022 October 22 (EG119B). In addition to the elements of the EVN, antennas of the e-MERLIN were also included in the VLBI network. Since the targets are faint sources, it was necessary to use the technique of phase referencing (Beasley & Conway 1995). With phase-referencing, in addition to increasing the coherent integration time on faint sources, we can also relate target positions to the known ICRF (Internatonial Celestial Reference Frame, Charlot et al. 2020) astrometric positions of the respective calibrator sources. In this observing mode, the radio telescopes were nodding between a nearby bright compact calibrator source and the given target, in repeating cycles. In our case, within the 8.5-min cycle time, 6.5 min was spent on the weak target source, the rest was spent on the calibrator and with antenna slewing. The EG119B run had a shorter, 7-min cycle time, of which 4.6 min was spent on the target source. The total bandwidth of 128 MHz was divided into four 32-MHz wide intermediate frequency channels (IFs), each further divided into 64 spectral channels. The data were recorded with 1024 Mbps data rate, in left and right circular polarizations. Bright compact fringe-finder sources were also scheduled in the experiments, J0646+4451, J1642+3948, and J2253+1608 in EG119A, and 3C 84 in EG119B. Overall, 15 radio telescopes participated in the experiments: Jodrell Bank Mk2 (38 m × 25 m diameter, United Kingdom), Westerbork (25 m, The Netherlands), Effelsberg (100 m, Germany), Medicina (32 m, Italy), Noto (32 m, Italy), Onsala (25 m, Sweden), Tianma (65 m, China), Urumqi (25 m, China), Toruń (32 m, Poland), Hartebeesthoek (26 m, South Africa) and the e-MERLIN antennas in the United Kingdom: Cambridge (32 m), Darnhall, Defford, Knockin, and Pickmere (25 m each). Urumqi participated in the EG119A experiment only. The data were processed at the Joint Institute for VLBI European Research Infrastructure Consortium (JIVE, Dwingeloo, The Netherlands) with the SFXC software correlator (Keimpema et al. 2015) with 2 s integration time. Typical (u, v) coverages for the two project segments are shown in Fig. 1.

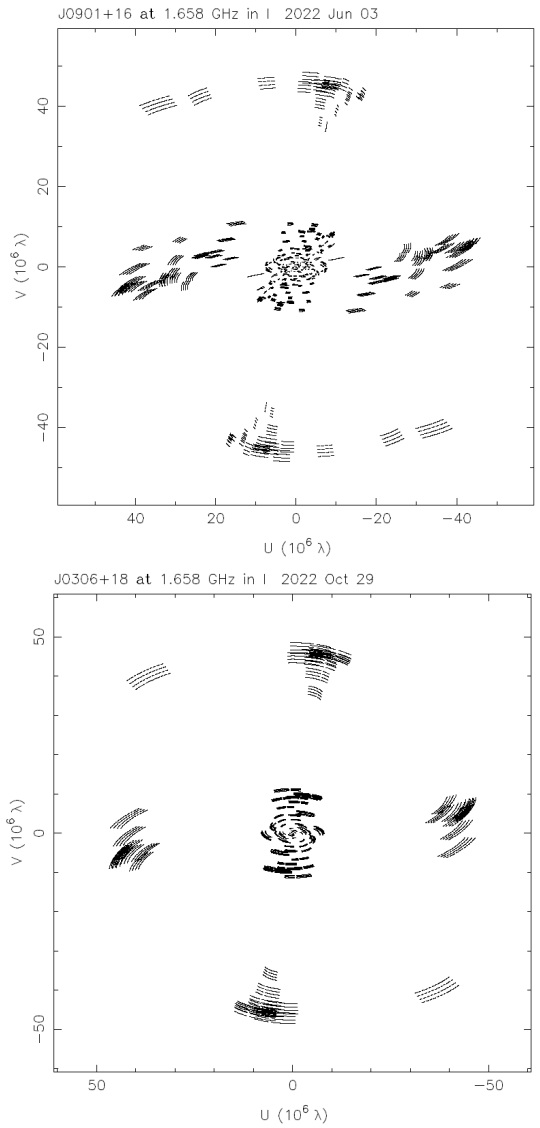

Fig. 1: Typical (u, v) coverages for low-declination targets in the EG119A (*top*) and EG119B (*bottom*) project segments.

3.2. Data reduction

The data were calibrated using the NRAO Astronomical Image Processing System (AIPS) software package (Greisen 2003), following a standard procedure (e.g. Diamond 1995). As the first step after loading the raw correlated data, the interferometric visibility amplitudes were calibrated using the antenna gain curves and the system temperatures measured at each telescope. Then, the data were corrected for the dispersive ionospheric delay using total electron content maps derived from global navigation satellite systems data. Phase changes due to the time variation of the source parallactic angle were also corrected for radio telescopes with azimuth–elevation mount. An initial correction of instrumental phases and delays was performed using a 1-min scan on a strong fringe-finder source. Then global fringe-fitting (Schwab & Cotton 1983) was performed on the phase-reference and fringe-finder calibrators. These calibrated

Table 1: Target sources and information on their respective phase-reference calibrators used in the EVN observations.

Source ID	z	$D_{\rm L}$ [Mpc]	Linear scale [pc mas^{-1}]	$S_{2.7}$ [mJy]	$S_{1.4}$ [mJy]	R [$L_{2.7\,\rm GHz}/L_{4400\,\rm A}$]	Phase calibrator	Separation [°]
J0306+1853	5.363[1]	50596	6.06	0.15 (0.01)*	...	0.9	J0259+1925	1.79
J0616−1338	5.580[2]	53030	5.94	1.3 (0.2)	...	9.3	J0618−1418	0.80
J0741+2520	5.194[3]	48767	6.16	4.2 (0.2)	2.9 (0.1)	6.5	J0746+2549	1.12
J0747+1153	5.260[4]	49493	6.12	1.5 (0.2)	...	8.6	J0749+1057	1.02
J0901+1615	5.630[5]	53585	5.91	2.9 (0.4)	3.9 (0.2)	76.1	J0905+1541	1.10
J1034+2033	5.010[6]	46748	6.28	3.9 (0.3)	3.9 (0.1)	20.4	J1036+2203	1.59
J1614+4640	5.313[6]	50077	6.09	4.0 (0.2)	1.7 (0.1)	20.3	J1616+4632	0.31
J2239+0030	5.090[6]	47624	6.23	1.0 (0.2)	1.4 (0.1)	29.9	J2239+0128	0.98
J2245+0024	5.170[6]	48393	6.18	1.4 (0.2)	0.9 (0.1)	58.0	J2247+0000	0.66
J2344+1653	5.000[6]	46638	6.28	10.5 (0.2)	...	24.3	J2347+1709	0.85

Notes. Col. 1 – source name derived from J2000 equatorial coordinates; Col. 2 – spectroscopic redshift and its reference in the upper index (1: Wang et al. (2015), 2: Yang et al. (2019), 3: McGreer et al. (2009), 4: Yang et al. (2016), 5: Bañados et al. (2015), 6: Wang et al. (2016)); Col. 3 – luminosity distance; Col. 4 – linear scale at the source redshift; Col. 5 – VLASS 2.7-GHz flux density (uncertainty in parentheses). * The 2.7-GHz flux density calculated using the spectral index from Sbarrato et al. (2021); Col. 6 – FIRST 1.4-GHz flux density (uncertainty in parentheses); Col. 7 – radio-loudness parameter; Col. 8 – phase-reference calibrator source name; Col. 9 – angular separation between the target and calibrator sources.

visibility data were exported to the DIFMAP software package (Shepherd et al. 1994), where we carried out hybrid mapping. The process involved several iterations of the CLEAN deconvolution algorithm (Högbom 1974) and phase-only self-calibration (Pearson & Readhead 1984), followed by a few rounds of amplitude and phase self-calibration with decreasing solution intervals. Antenna-based median gain correction factors, if in excess of ±5%, were applied to the visibility amplitudes in AIPS. The CLEAN model components of the calibrators produced in DIFMAP were transferred to AIPS as inputs for a repeated fringe-fitting of the calibrator data. By taking the phase-reference calibrator source structure into account, we could improve phase solutions. The fringe-fit solutions obtained for the phase-reference calibrators were interpolated to the respective target source data. The calibrated visibility data of the target sources were then exported from AIPS.

The final target source images were produced with DIFMAP (Shepherd et al. 1994). To reduce the image noise, we applied natural weighting, where weights were calculated as the reciprocal of the amplitude errors (UVWEIGHT 0, −1). The dirty images were shifted to make the brightness peak coincide with the origin at (0,0) relative right ascension and declination. Following a standard mapping procedure for weak (mJy-level) targets, only a few rounds of CLEAN iterations were performed without self-calibration. After reaching an insignificant peak-to-noise level (below $\sim 5\sigma$) in the residual images, we performed a final CLEAN iteration involving 1000 steps with a very small loop gain (0.01). The purpose of this last step is to smooth the noise features in the final images. The resulting images are presented in Fig. 2 and their parameters are listed in Table 2. The phase-referenced VLBI positions of the sources were obtained from the images using the AIPS task MAXFIT.

The e-MERLIN stations participating in the interferometer network provided relatively short baselines and thus allowed us to check whether there is ∼ 100-mas scale extended emission in our sources. In DIFMAP, we applied a taper to the visibility data to reduce the weight of the longer baselines (UVTAPER 0.5, 12). This way we increased the sensitivity to detect possible extended emission. We set the full width at half maximum (FWHM) of the Gaussian taper at the baseline length of 12 million wavelengths (Mλ).

In addition to producing the CLEAN images, circular Gaussian brightness distribution model components were also fitted to the visibility data (Pearson 1995) in DIFMAP. This allowed us to quantitatively characterise component sizes and flux densities (Table 3). In the absence of self-calibration, the effect of coherence loss (Martí-Vidal et al. 2010) on the peak brightness and flux density values has to be considered. To estimate the level of correction for coherence loss, we imaged and modelled the calibrator sources with and without performing phase self-calibration, and found an average model flux density difference of 25%. Therefore, the fitted flux densities and the peak brightness values were multiplied by a factor of 1.25. This factor can still be considered as a lower limit because it does not take into account the fact that the calibrator data have been fringe fitted, and their visibility phases are already corrected to a better degree than for the targets. Note that our correction factor is consistent with estimates found for other EVN experiments (e.g. Mosoni et al. 2006; Gabányi et al. 2019; Krezinger et al. 2022).

The uncertainties of the parameters of the fitted Gaussian model components were estimated following the method of Fomalont (1999). For the flux densities, an additional 5% error was added in quadrature, to account for the VLBI absolute amplitude calibration uncertainty (e.g. An et al. 2012; Frey et al. 2015).

4. Results

The naturally weighted 1.7-GHz EVN images are presented in Fig. 2. The image parameters are listed in Table 2. Out of the ten target sources, nine were successfully detected as a compact core. The tapering described in Sect. 3.2 did not reveal extended emission around any of the compact cores in the detected 9 sources. Only three (namely J1034+2033, J1614+4640, and J2344+1653) of the brighter sources cloud be imaged at higher resolution with applying uniform weighting. J0306+1853 was found to be non-detected even after applying different data weighting schemes and tapering. The upper limit to the brightness of this source is 113 μJy beam^{-1} (5 σ) using the same natural weighting applied for the images in Fig. 2 and corrected for 25% coherence loss. The parameters derived for the sources are given in Table 3.

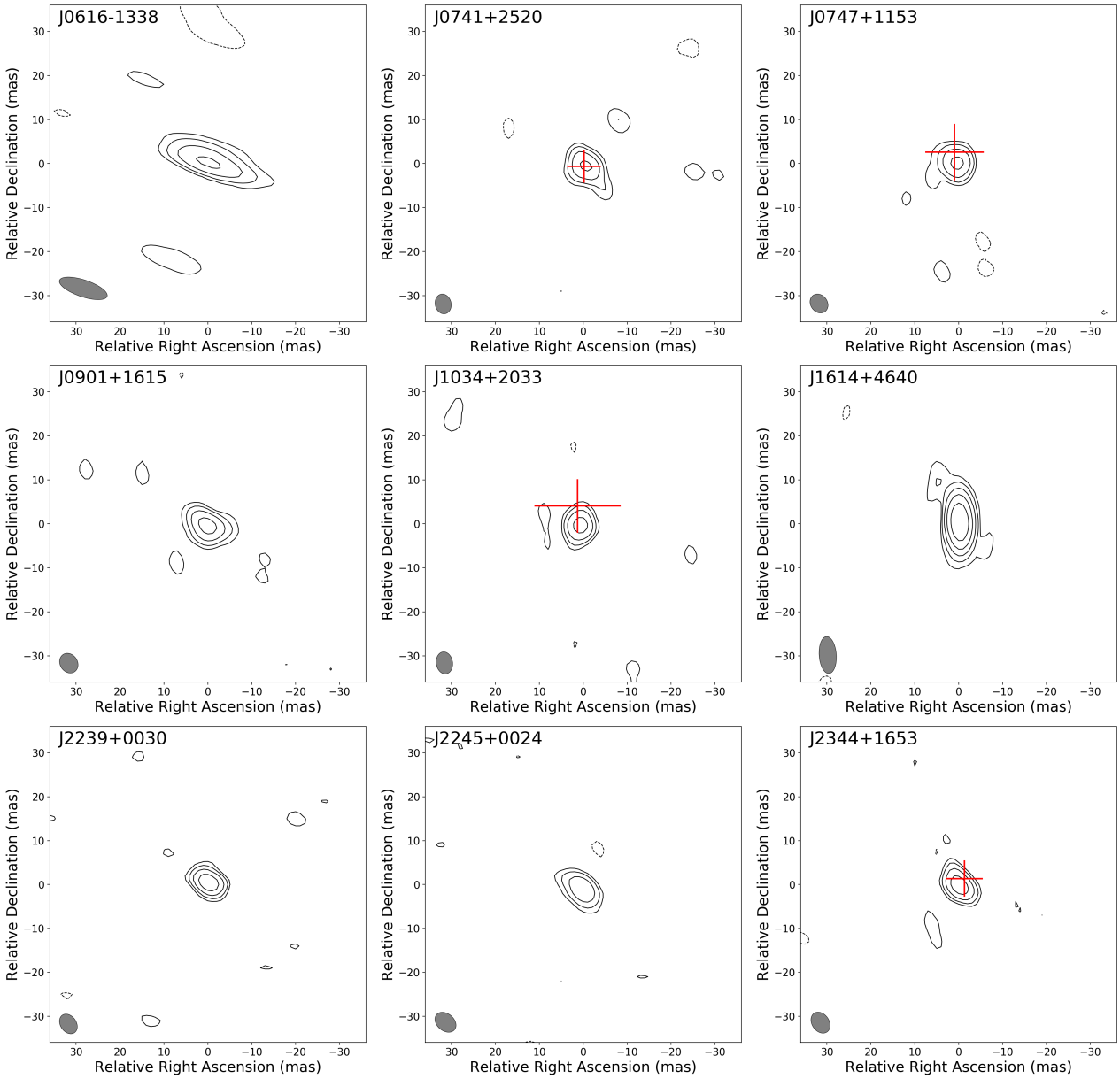

Fig. 2: Naturally weighted EVN images at 1.7 GHz. Red crosses mark the *Gaia* DR3 optical position in the four cases where it is available. The size of the crosses indicates the $3\sigma_{\rm pos}$ uncertainty (see Sect. 5.2). The lowest contours are drawn at ±3 times the image noise and the positive contours increase by a factor of 2. The restoring beam is shown in the bottom-left corner. Table 2 contains the image parameters and the coordinates corresponding to the images centres.

The 1.7-GHz redshift-corrected brightness temperatures were calculated following (Condon et al. 1982):

$$T_{\rm b} = 1.22 \times 10^{12}\,(1+z)\frac{S_\nu}{\theta^2\nu^2}\ \ [\rm K], \tag{1}$$

where z is the redshift, S_ν the integrated flux density of the core in Jy, θ the fitted circular Gaussian component diameter (FWHM) in milliarcsecond, and ν the observing frequency in GHz. To check whether the sources are resolved by the interferometer, we calculated the minimum resolvable size following the formula of Kovalev et al. (2005). We found that each of our sources are resolved. It should be noted here that the slightly resolved structure could also be partly an effect of visibility phase decorrelation.

To investigate the compactness of the sources on the VLBI scale, we adopted the method presented by Lee et al. (2008). They define the compactness as the ratio of the core flux density to the total flux density of the CLEAN components obtained during the imaging, $S_{\rm core}/S_{\rm clean}$. Here $S_{\rm core}$ is equal to the modelled flux density, $S_{1.7}$, while $S_{\rm clean}$ is obtained by integrating the flux density contained in the CLEAN components in a 15-mas radius region around the core. The $S_{\rm clean}$ values are consistent with the modelled flux densities within 10%, which indicates that the sources are core-dominated, as seen from their appearance in the VLBI images (Fig. 2).

Another way to characterise the compactness of the sources is to investigate the ratio of their VLBI flux density to the total flux density. However, this indicator gives information about the difference in the radio emission between parsec and kiloparsec scales. We calculated the ratio of the 1.7-GHz VLBI flux density obtained from Gaussian model fits ($S_{1.7}$) to the total flux

Table 2: 1.7-GHz VLBI image parameters and source positions.

Source ID	RA_{VLBI} [h min s]	Dec_{VLBI} [° ′ ″]	Peak intensity [mJy beam^{-1}]	Restoring beam [mas × mas]	[°]	1σ noise [mJy beam^{-1}]
J0616−1338	06 16 24.37784 (0.00016)	−13 38 06.4239 (0.0024)	1.08 (0.09)	11.4 × 3.8	71.5	0.04
J0741+2520	07 41 54.71629 (0.00008)	+25 20 29.5594 (0.0012)	0.81 (0.06)	4.6 × 3.6	13.4	0.03
J0747+1153	07 47 49.17454 (0.00008)	+11 53 52.4652 (0.0012)	0.76 (0.06)	4.6 × 3.8	37.2	0.03
J0901+1615	09 01 32.64577 (0.00008)	+16 15 06.7575 (0.0012)	1.15 (0.08)	4.7 × 3.9	34.3	0.04
J1034+2033	10 34 18.64033 (0.00009)	+20 33 00.1247 (0.0013)	1.68 (0.12)	5.1 × 3.7	8.8	0.05
J1614+4640	16 14 25.14299 (0.00013)	+46 40 28.9963 (0.0019)	2.57 (0.10)	8.4 × 3.9	4.0	0.03
J2239+0030	22 39 07.56146 (0.00008)	+00 30 22.5944 (0.0012)	0.78 (0.06)	4.9 × 3.6	34.8	0.02
J2245+0024	22 45 24.27741 (0.00009)	+00 24 14.1389 (0.0013)	0.45 (0.04)	5.4 × 3.9	49.8	0.02
J2344+1653	23 44 33.49974 (0.00009)	+16 53 16.5598 (0.0013)	3.36 (0.23)	5.2 × 3.9	34.7	0.10

Notes. Col. 1 – source name; Col. 2 – right ascension with its uncertainty in seconds (in parentheses); Col. 3 – declination with its uncertainty in arcseconds (in parentheses); Col. 4 – image peak intensity; Col. 5 – restoring beam major and minor axes (FWHM); Col. 6 – position angle of the restoring beam major axis, measured from north through east; Col. 7 – 1σ image noise level.

density ($S_{\rm VLA,1.7}$). The latter values are estimated using the derived spectral indices or log-parabolic spectral fits (see more in Section 5.3).

Using the formula of Hogg et al. (2002), we calculated the core and total 1.7-GHz redshift-corrected monochromatic radio powers, $P_{1.7,\rm core}$ and $P_{1.7,\rm total}$, respectively:

$$P_\nu = 1.20 \times 10^{20}\, D_{\rm L}^2 S_\nu (1+z)^{-1-\alpha}\ [\rm W\,Hz^{-1}]. \quad (2)$$

In this equation, $D_{\rm L}$ refers to the source luminosity distance in Megaparsec unit, α is the radio spectral index (see Table 4), and $S_\nu = S_{1.7}$ for $P_{1.7,\rm core}$ (assuming the same spectral index for the VLBI-scale emission as derived from the total flux densities), while $S_\nu = S_{\rm VLA,1.7}$ for $P_{1.7,\rm total}$. We applied $\alpha = 0$ to sources with peaked spectrum because the spectral shape in the frequency range where the K-correction is applied is close to flat (see Fig. 3).

5. Discussion

5.1. The origin and the nature of the radio emission

The high detection rate of compact parsec-scale jets in RQQs in this study (three sources out of four were detected) contrasts with the low detection rates seen in low-redshift RQQ samples (Baldi et al. 2018, 2021; Wang et al. 2023a,b). This potentially suggests an interesting evolution in the jet properties and/or launch mechanisms of RQQs with cosmic time. Selection effects still could play a role in this contradiction. It should be noted when the results are compared with the low-redhsift samples that the rest-frame frequencies for our 1.7-GHz measurements at $5 < z < 6$ are equal to $\sim 10 - 12$ GHz. The difference between the rest-frame frequencies could cause bias in the comparison. Nevertheless, the detected sources may represent the tip of the iceberg, the brightest, most luminous of the high-redshift RQQ population. Further deeper VLBI observations probing fainter sources would test whether the high detection rate holds. It is possible that the RLQ/RQQ dichotomy itself becomes increasingly blurred at high redshifts, if a larger fraction of AGN have relativistic jets due to different accretion physics or environmental conditions in the early Universe.

The sources detected in our sample appear to be highly core-dominated. They seem to lack extended emission due to the losses coming from scattering with cosmic microwave background (CMB) photons (Ghisellini et al. 2015a), or perhaps the parsec-scale jets are beamed towards the observer. It is also possible that these radio AGN are very young, powerful, and intrinsically small sources (O'Dea & Saikia 2021). The derived brightness temperatures (see Table 3) all exceed $T_{\rm b} = 10^6$ K by at least two orders of magnitude, clearly indicating non-thermal radio emission related to AGN activity and ruling out star formation in the host galaxy as the primary source of radio emission (Condon 1992; Kewley et al. 2000; Middelberg et al. 2011). The AGN-associated activity may include jets, outflows and coronal emission (Panessa et al. 2019). The compactness and the derived $T_{\rm b} \sim 10^{8-9}$ K values strengthen the case for the presence of plasma jets in our sources. Jetted radio sources often show relativistically enhanced radio emission, depending on the jet inclination to the line of sight and the bulk speed of the plasma. The jet emission is considered Doppler-boosted when $T_{\rm b}$ exceeds the equipartition value of $T_{\rm b,eq} \approx 5 \times 10^{10}$ K (Readhead 1994). Having the highest measured $T_{\rm b} = (5.3 \pm 0.9) \times 10^9$ K in our sample, the radio emission in none of these sources appears Doppler-boosted, suggesting their jets are not aligned close to the line of sight. However, VLBI imaging at higher observing frequency and thus with better angular resolution might be able to reveal higher brightness temperatures in these sources, depending on the shape of the radio spectrum.

The parsec-scale morphology of the radio structures in this sample of nine VLBI-detected AGN is generally similar to what is seen in other high-redshift VLBI samples (e.g. Coppejans et al. 2016; Krezinger et al. 2022). There is no clear sign of extended emission beyond a few mas radius or other jet component in addition to the compact core. The only exception is J2344+1653, where the $S_{1.7}/S_{\rm VLA,1.7}$ ratio is 0.50 ± 0.08. It suggests the presence of a diffuse ($\sim 0.1 - 1''$) emission around the compact core which is resolved out by the EVN. This could also apply for J2245+0024, but the uncertainties are larger for that source (Table 3).

5.2. Gaia optical astrometric positions

The *Gaia* astrometric space mission provides the most accurate optical positions available nowadays for AGN (Gaia Collaboration et al. 2016, 2023). Thanks to the sensitivity of *Gaia*, its catalogue contains even some faint distant AGN. Comparing their coordinates with the radio positions derived from VLBI observations which have similar (milliarcsecond or sub-milliarcsecond) accuracy, additional information on the nature of the investigated sources could be revealed. The optical position of a quasar is generally linked to the thermal emission originating from the accretion disk (Kovalev et al. 2017; Plavin et al. 2019), or sometimes to synchrotron emission of bright optical jets (e.g. Lambert et al. 2024). For high-redshift quasars like our target sources, the

Table 3: Derived physical parameters of the sources.

Source ID	$S_{1.7}$ [mJy]	$\theta_{1.7}$ [mas]	$T_{b,1.7}$ [10^8 K]	S_{clean} [mJy]	$S_{VLA,1.7}$ [mJy]	$S_{1.7}/S_{VLA,1.7}$	$P_{1.7,core}$ [10^{26} W Hz^{-1}]	$P_{1.7,total}$ [10^{26} W Hz^{-1}]
J0306+1853	$< 0.11^*$	...	...	...	0.23 (0.01)	...	...	0.57 (0.08)
J0616−1338	1.86 (0.27)	2.3 (0.1)	10.6 (2.0)	1.86	...	...	3.86 (0.73)	...
J0741+2520	2.69 (0.36)	8.5 (0.5)	1.0 (0.2)	2.54	3.33 (0.41)	0.81 (0.21)	1.24 (0.22)	1.54 (0.26)
J0747+1153	1.79 (0.24)	4.0 (0.2)	3.1 (0.6)	1.81	...	...	1.66 (0.29)	...
J0901+1615	3.06 (0.39)	8.4 (0.5)	1.3 (0.2)	3.19	3.68 (0.17)	0.82 (0.15)	3.96 (0.70)	4.75 (0.62)
J1034+2033	3.46 (0.46)	3.2 (0.2)	9.2 (1.6)	3.56	4.18 (0.14)	0.83 (0.14)	1.51 (0.27)	1.83 (0.22)
J1614+4640	3.45 (0.35)	1.5 (0.1)	41.7 (4.9)	3.96	2.95 (0.41)	1.23 (0.29)	1.73 (0.27)	1.41 (0.29)
J2239+0030	1.36 (0.18)	2.2 (0.1)	7.7 (1.4)	1.56	1.06 (0.21)	1.28 (0.42)	1.06 (0.19)	0.83 (0.19)
J2245+0024	0.76 (0.12)	4.0 (0.3)	1.3 (0.3)	0.76	1.31 (0.14)	0.58 (0.16)	0.35 (0.07)	0.60 (0.09)
J2344+1653	7.03 (0.89)	1.9 (0.1)	53.0 (8.9)	6.67	14.13 (0.47)	0.50 (0.08)	9.31 (1.61)	18.71 (2.27)

Notes. * non-detection, an upper limit to the peak brightness is given in mJy beam^{-1}; the errors are shown in parentheses; Col. 1 – source name; Col. 2 – 1.7-GHz fitted core flux density, with errors shown in parentheses; Col. 3 – fitted FWHM of the core component; Col. 4 – redshift-corrected 1.7-GHz brightness temperature; Col. 5 – CLEANed flux density integrated within the central 15-mas radius area; Col. 6 – 1.7-GHz total flux density estimated using the derived spectral indices and log-parabolic coefficients (see Table 4); Col. 7 – ratio of the measured VLBI and the calculated total 1.7-GHz flux densities; Col. 8 – 1.7-GHz monochromatic radio power for the core and its uncertainty; Col. 9 – 1.7-GHz total monochromatic radio power and its uncertainty.

redshift is determined using broad Lyα lines formed in the broad-line region (BLR) in the vicinity of the central black hole (Peterson 2006). In case of a dominant non-thermal optical emission from the relativistic jet, the thermal component from the BLR would be suppressed. Therefore, the detection of the broad emission lines in the optical spectra of high-redshift quasars favours the thermal origin of their optical emission. On the other hand, the radio emission corresponds to the synchrotron self-absorbed base of the jet (i.e. the radio core) with $\tau_\nu = 1$ optical depth at the given frequency ν, or possibly a compact hotspot associated with a shock front between the jet and the surrounding medium. The radio core is usually the brightest and most compact region of the jet and can be pinpointed with VLBI observations (e.g. Fey et al. 1997). Up to a few milliarcsecond offset between radio and optical AGN positions can occur and its position angle is found to statistically coincide with the VLBI jet direction (Petrov et al. 2019). For faint radio sources like the typical high-redshift quasars, revealing a significant *Gaia*–VLBI positional mismatch exceeding the typical values could help constraining the source classification and the nature of compact radio emission, as it would suggest an extended structure with a quasar jet misaligned with respect to the line of sight.

Out of the ten targets in our sample, five (namely J0306+1853, J0741+2520, J0747+1153, J1034+2033, and J2344+1653) have been detected by *Gaia*. We looked for counterparts for the remaining five sources in the *Gaia* source catalogue, but there were no matches within $\sim 1''$ angular distance. The *Gaia* positions are marked with red crosses in Fig. 2. The uncertainties of the optical positions from the *Gaia* DR3 (Gaia Collaboration et al. 2023) are within 3 mas. The astrometric excess noise is only significant in the case of J0747+115, where we added it to the formal position error in quadrature. Since the quasar J0306+1853 remained undetected with the EVN, we could not derive its accurate radio position to be compared with the *Gaia* position.

The VLBI astrometric positions determined for our targets by phase-referencing to nearby calibrator sources can be considered as linked to the ICRF (Charlot et al. 2020). Our measured *Gaia*–VLBI positional offsets are ranging between 1.3 − 1.8 mas. However, ICRF positions refer to X band (8.4 GHz), while our phase-referenced observations were carried out at L band (1.7 GHz). The frequency-dependent core shift in a synchrotron self-absorbed jet can amount $\sim$ 1 mas between these frequencies (e.g. Sokolovsky et al. 2011). Moreover, according to Porcas (2009), there could be up to $\sim$ 0.2-mas offset between the phase-referenced and group-delay positions along the jet direction, caused by opacity effects on the emission at the jet base. An offset can be considered significant if the optical position differs by more than $3\sigma_{pos}$, where $\sigma_{pos} = \sqrt{\sigma^2_{VLBI} + \sigma^2_{Gaia}}$, the square root of the sum of squares of the VLBI and the *Gaia* positional uncertainties. Based on this criterion, we find the optical–radio offsets insignificant. This in fact indicates that the detected radio features could be related to the inner jet, located close to the central engine.

5.3. Continuum radio spectra

We collected the available single-dish and low-resolution radio interferometric observations from the literature for the targets, in order to build their total flux density spectra. The investigated quasars are faint ($S_{2.7} < 11$ mJy, Table 1), thus they are often below the detection thresholds of shallow surveys. The main sources of the flux density measurements are the GMRT (Giant Metrewave Radio Telescope) and uGMRT (upgraded GMRT) observations of radio-loud quasars at $z > 5$ (Shao et al. 2020, 2022) and various surveys carried out with the VLA (Table 4). The continuum spectra for the ten sources in our sample are shown in Fig. 3. There are two objects, J0616−1338 and JJ0747+1153, where only the 2.7-GHz VLASS measurements are available. For the rest of the sample, we fitted the spectral data points to characterise their continuum spectrum (black-coloured fits in Fig. 3). In four cases, we assumed a power-law radio spectrum $S \propto \nu^\alpha$, where S is the flux density, ν the frequency, and α the spectral index. Power-law spectra are called steep if $\alpha < -0.5$, flat if $-0.5 \leq \alpha \leq 0$, and inverted if $\alpha > 0$. In the case of four sources (J0741+2520, J1034+2033, J1614+4640, and J2245+0024) with an apparently curved spectral shape, we found that the choice of a log-parabolic function in the form of $\log S = a(\log \nu - \log\ \nu_0)^2 + b$ resulted in lower χ^2 values than using the power-law function. In the formula above, ν_0 is the turnover frequency corresponding to the peak flux density S_0, while a and b are numerical constants (e.g. Coppejans et al. 2017). The log-parabolic fit can be characterised by the

ν_0 and S_0 values. Given that some sources in our sample lack low-frequency data points, it is possible that the their spectra are in fact also peaked. Peaked continuum radio spectra seem to be common for bright $z > 3$ radio quasars (Sotnikova et al. 2021). Also, Shao et al. (2022) found that $z > 5$ radio-loud quasars tend to show evidence for spectral turnover at rest-frame frequencies of $\sim 1 - 50$ GHz.

In Table 4, we give the flux densities and the derived spectral parameters, i.e. the spectral indices in the case of power-law fits, and the peak frequency (ν_0) and flux density (S_0) values for log-parabolic fits. Out of the four sources whose flux densities versus frequency are best described with a power-law function, two show flat and two steep spectrum. The four peaked spectra have their maxima between $1 - 5$ GHz which corresponds to $\sim 6 - 30$ GHz in the rest frame of the sources. The fitted ν_0 and S_0 values are consistent within the uncertainties with the results of Shao et al. (2022) who also found these sources having peaked spectra. The difference between our and their analyses is that we also included the 1.4-GHz FIRST and 2.7-GHz VLASS data points.

Deriving spectral indices of the compact VLBI components would require VLBI measurements in at least two different frequency bands taken preferably at around the same time, to avoid possible effects of variability. If the source is compact enough that the VLBI flux density is comparable to the low-resolution measurements, the VLBI flux density can be included in the total flux density spectral analyses to help constrain the fit. We found the compactness of J0616−1338 and J0747+1153 to be close to unity (Table 3), therefore we used our 1.7-GHz EVN measurements together with the 2.7-GHz VLASS data to derive their spectral index (red-coloured fits in Fig. 3). J0616−1338 has steep spectrum with $\alpha^{2.7\ \mathrm{GHz}}_{1.7\ \mathrm{GHz}} = -0.72 \pm 0.49$, although the large uncertainty allows for a flat spectrum as well. J0747+1153 has formally a flat spectrum, but the uncertainty is also large because there are only two spectral points available, at relatively close frequencies.

5.4. Variability

Variability is an indicator of relativistic jet or coronal emission for radio-quiet AGN (e.g. Wang et al. 2023b) and of powerful jets in high-redshift radio-loud AGN (e.g. Sotnikova et al. 2024). Due to the lack of measurements performed at the same frequencies and with similar angular resolution in multiple observing epochs, our ability the investigate flux density variability is limited. However, the targets can be investigated by comparing the high-resolution VLBI flux densities with single-dish and low-resolution radio interferometric data. It should be noted that the estimated total flux density values themselves may be affected by long-term variability since the measurements at different frequencies used to determine the spectral shapes and spectral indices were not simultaneous. If $S_{1.7}/S_{\mathrm{VLA},1.7} > 1.1$, we consider the source variable. Only two of the sources (J1614+4640 and J2239+0030) fulfil this criterion, although the large uncertainties make the possible variabilities indefinite. The possible explanation for ratios below 0.9 is that a significant fraction of the total radio emission originates from an extended region resolved out with VLBI. Nevertheless, variability cannot be ruled out in these cases, just the data available at present are not sufficient to claim it.

Krezinger et al. (2022) found about half of their 13 targets in a $4 \lesssim z \lesssim 4.5$ radio quasar sample to be variable, while in a larger $z > 4.5$ sample containing the then-known 30 VLBI-detected source, Coppejans et al. (2016) concluded that only about 20% of the targets are significantly variable. In recent studies, Wang et al. (2023a,b) investigated RQQs and RLQs at $z \lesssim 0.5$ and found that core-dominated RQQs with flat/inverted spectrum have more pronounced variability, while steep-spectrum jet-dominated RQQs show negligible variability. Our findings, albeit limited by the available data, do not contradict with the findings cited above.

5.5. The non-detection of J0306+1853

J0306+1853 remained undetected in our EVN–e-MERLIN observation. Earlier, Sbarrato et al. (2021) observed this source with the VLA at 1.5 and 5 GHz. At both frequencies, they found the source unresolved with point-like structure on arcsecond scale. The derived spectral index (-0.87 ± 0.06, see also our Table 4) indicates a steep spectrum and thus an extended structure. However, the VLA detection raised the possibility of the presence of a sub-arcsecond compact jet structure. The radio loudness $R_{4400\text{Å}} = 0.7$ (Sbarrato et al. 2021) indicates that the source is radio-quiet. The sensitivity of the EVN observation allowed us to reach 113 μJy beam^{-1} (5 σ) detection limit, which would have been sufficient to detect a milliarcsecond-scale compact source with the 1.5-GHz VLA flux density of 252 μJy with a signal-to-noise ratio of ~ 10. Based on our non-detection, the radio emission of J0306+1853 is apparently resolved out on milliarcsecond to $\sim 0\farcs1$ angular scales. It seems less likely but still possible that J0306+1853 is variable.

5.6. The radio loudness–brightness temperature relation at high redshift

There are two commonly used definitions of the radio-loudness parameter. Kellermann et al. (1989, 2016) defined $R_{4400\text{Å}}$ as the fraction of the rest-frame 5-GHz radio and the optical power at 4400 Å. On the other hand, Sramek & Weedman (1980) defined $R_{2500\text{Å}}$ based on the 2500 Å optical power. To investigate the relation between radio loudness and other physical parameters, focusing on high-redshift quasars, we collected all the available $z > 5$ sources from the literature, altogether 48 objects, which have either any radio-loudness index ($R_{4400\text{Å}}$ or $R_{2500\text{Å}}$) published, or L-band (1.4 − 1.7 GHz) VLBI observation available, or both. SMBH masses were also collected from the literature where available, for about one third of the sample. We found that the mean M_{SMBH} at $z > 5$ is 4.4×10^9 M$_\odot$ All the collected sources are listed in Table A.1 with their radio-loudness indices, brightness temperature, SMBH mass, L-band flux densities and monochromatic powers, along with the respective references. The choice of the L band is motivated by the fact that this is the most commonly used frequency band for $z > 5$ quasar VLBI observations, and this way we can also include our nine newly-detected sources in the sample.

For the VLBI observations, we took data and references from Table 1 of Krezinger et al. (2022) as a starting point, and collected the derived redshift-corrected brightness temperatures. We extended this sample with the few sources that have been published since then: VIK J2318−3113 (Zhang et al. 2022), J0141−5427 (Gabányi et al. 2023), and J1702+1301 (Liu et al. 2024). There are currently 24 sources known with L-band VLBI observations, including the nine presented in this paper. Out of these 24 sources, seven have only lower limit to T_b. Each source has a single epoch of observation. The bottom left panel in Fig. 4 shows the L-band brightness temperatures as a function of redshift. The median T_b is $5.9{\times}10^8$ K. The measured T_b values show

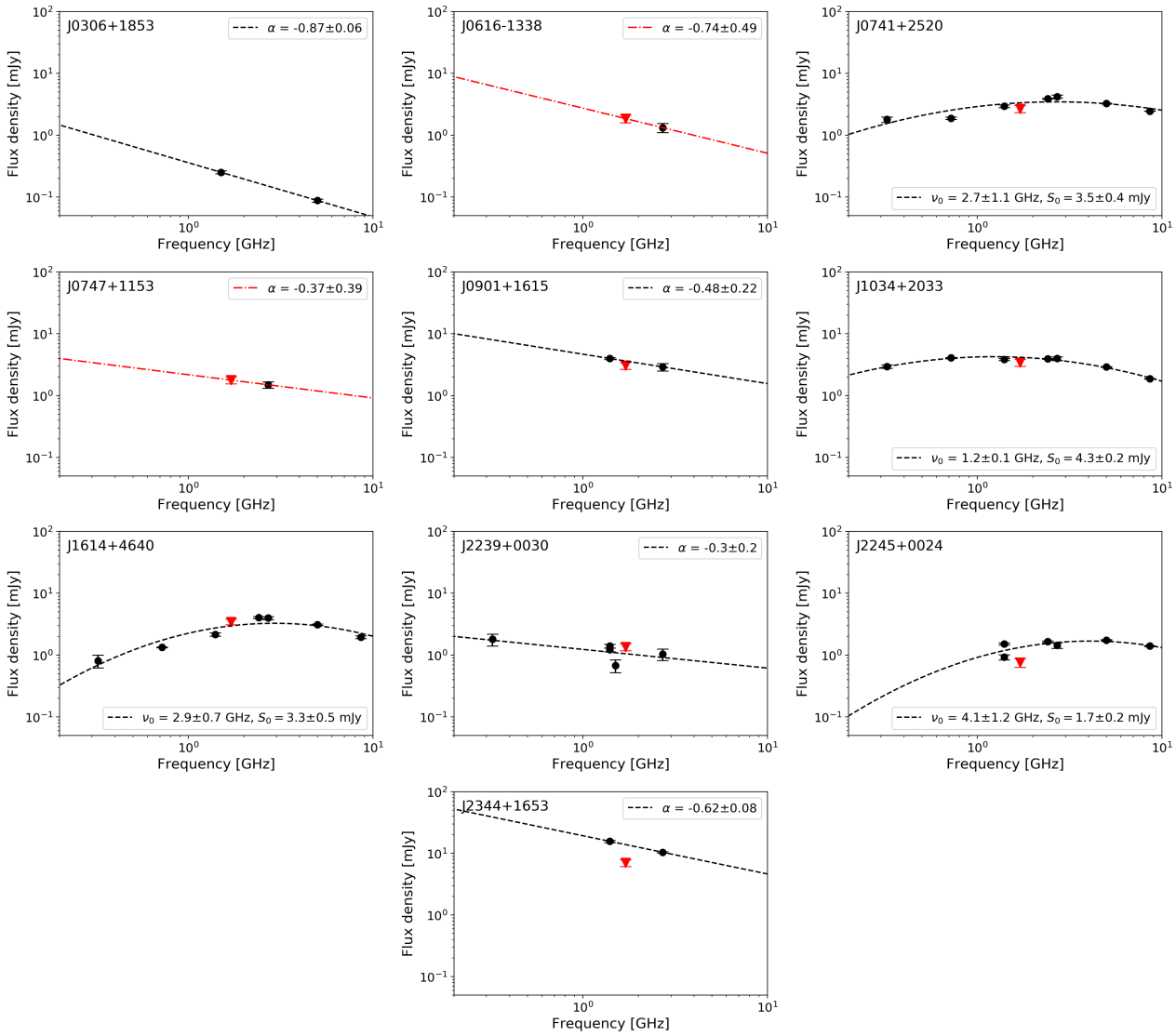

Fig. 3: Radio continuum spectra of the ten sources in our sample. Black points indicate total flux density data from single-dish and low-resolution interferometric measurements. The black dashed lines show the best-fit spectrum (power-law or log-parabolic). The parameters of the spectral fits are given in the insets and listed in Table 4. The red data points are the 1.7-GHz EVN flux density measurements presented in this paper. The red dashed-dotted lines for J0616−1338 and J0747+1153 show the power-law function fitted to the only available two flux density data points (VLASS and EVN), with the assumption that all the radio emission is confined to a small spatial scale corresponding to the compact VLBI component.

a generally decreasing trend with increasing redshift. Also, the jet emission of only a small fraction of these sources appears Doppler-boosted ($T_b \gtrsim 5 \times 10^{10}$ K) at L-band.

We found 43 sources with published $R_{4400Å}$ and 23 sources with $R_{2500Å}$ values, with 21 overlapping objects. In the cases where multiple R values are published for a given source, we considered the value published most recently. Because of variability, the R value may depend on the epochs when the luminosities were measured. It is usually not feasible to measure the radio and optical luminosities at the same time. Therefore strong variability of certain sources can influence the R indices when there are optical magnitudes or radio flux density measurements available at different epochs. Another uncertainty of R is caused by the choice of spectral indices assumed when performing K-correction, i.e. calculating the rest-frame 5-GHz or 4400 Å luminosities. Considering all these caveats, it is not surprising to find occasionally very different R values in the literature for many sources. However, the plot showing $R_{2500Å}$ as a function of $R_{4400Å}$ values (top left panel of Fig. 4) for the $z > 5$ sources where both values are available indicates that in most cases the values of the two radio-loudness indices are not markedly different. This justifies their use together when analysing the general properties of the sample.

The top right panel of Fig. 4 displays the distribution of T_b as a function of radio-loudness parameters $R_{4400Å}$ and $R_{2500Å}$. Based on this plot, a general trend of increasing brightness temperature with increasing radio loudness can be seen. It appears that, despite the uncertainties described above, the sources with higher R index have higher T_b in L band. Since the radio loudness is proportional to the total flux density and the brightness temperature to the core flux density (Eq. 1), the existence of such a relation is not surprising if the radio emission is confined to the compact AGN core region. Populating the parameter space where the coverage is more incomplete (i.e. $R < 10$ and

Table 4: Total flux density data used collected from the literature.

Source ID	α	$S_{323\ \mathrm{MHz}}$ [mJy]	$S_{720\ \mathrm{MHz}}$ [mJy]	$S_{1.4\ \mathrm{GHz}}$ [mJy]	$S_{2.4\ \mathrm{GHz}}$ [mJy]	$S_{2.7\ \mathrm{GHz}}$ [mJy]	$S_{5\ \mathrm{GHz}}$ [mJy]	$S_{8.6\ \mathrm{GHz}}$ [mJy]
J0306+1853	−0.87 (0.08)			0.25 (0.01)[1]			0.09 (0.01)[1]	
J0616−1338	−0.74 (0.49)*					1.33 (0.22)		
J0741+2520	S_0 = 3.5 (0.4)	1.80 (0.19)[4]	1.89 (0.08)[5]	2.97 (0.14)[3]	3.27 (0.03)[5]	4.23 (0.24)[2]	3.89 (0.05)[5]	2.46 (0.02)[5]
	ν_0 = 2.7 (1.1)							
J0747+1153	−0.37 (0.39)*					1.50 (0.17)[2]		
J0901+1615	−0.48 (0.22)			3.99 (0.15)[3]		2.92 (0.41)[2]		
J1034+2033	S_0 = 4.3 (0.2)	2.97 (0.19)[4]	4.08 (0.07)[5]	3.85 (0.14)[3]	3.94 (0.06)[5]	3.99 (0.29)[2]	2.92 (0.04)[5]	1.88 (0.03)[5]
	ν_0 = 1.2 (0.1)							
J1614+4640	S_0 = 3.3 (0.5)	0.81 (0.19)[4]	1.34 (0.01)[5]	2.16 (0.14)[3]	4.06 (0.16)[5]	4.00 (0.23)[2]	3.13 (0.08)[5]	1.96 (0.10)[5]
	ν_0 = 2.9 (0.7)							
J2239+0030	−0.31 (0.19)	1.80 (0.39)[4]		1.40 (0.10)[3]		1.04 (0.22)[2]		
				1.22 (0.08)[6]				
				0.68 (0.16)[7]				
J2245+0024	S_0 = 1.7 (0.2)			0.93 (0.09)[3]	1.65 (0.06)[5]	1.44 (0.15)[2]	1.75 (0.03)[5]	1.40 (0.03)[5]
	ν_0 = 4.1 (1.2)			1.52 (0.06)[6]				
J2344+1653	−0.62 (0.08)			15.7 (0.7)[8]		10.12 (0.24)[2]		

Notes. * two-point spectral index derived from 1.7-GHz VLBI and 2.7-GHz VLASS flux density measurements; Col. 1 – source designation; Col. 2 – fitted power-law spectral index; where log-parabolic function was fitted, we give values S_0 in mJy and ν_0 in GHz; Col. 3–9 – flux densities at the various frequencies and their uncertainties collected from the literature; numbers in the upper indices are references to the measurements: 1: Sbarrato et al. (2021), 2: VLASS, 3: FIRST, 4: Shao et al. (2020), 5: Shao et al. (2022), 6: Hodge et al. (2011), 7: Heywood et al. (2016), and 8: Condon et al. (1998).

$R > 100$), this relation could be constrained further. The high-redshift regime of the $R - z$ diagram started to be built up in the recent years (Belladitta et al. 2019; Bañados et al. 2021), with more and more distant extragalactic radio sources identified. The bottom right panel of Fig. 4 shows the $R_{4400\text{Å}}$ and $R_{2500\text{Å}}$ (where there was no available $R_{4400\text{Å}}$ value) indices of AGN at $z > 5$ as a function of redshift. The median values of the collected $R_{4400\text{Å}}$ and $R_{2500\text{Å}}$ indices are are 35 and 90, respectively.

5.7. The radio power distribution at high redshift

The derived core and total monochromatic radio powers of our sources at 1.7 GHz are in the range of $\sim 10^{25-27}$ W Hz^{-1}. These radio powers are typical of Fanaroff–Riley type II (FRII, Fanaroff & Riley 1974) radio galaxies and quasars, spanning from the low-end to the the high-power regime (e.g. Giovannini et al. 2001; Giovannini 2004; Sbarrato et al. 2021). The phenomenological division line between FRI and FRII sources is at $P_{\mathrm{total}} \approx 10^{25}$ W Hz^{-1} (Fanaroff & Riley 1974), but it is based on low-frequency observations. It appears that while these sources can be classified as radio-quiet, they in fact have radio powers typical of a 3C radio galaxy, i.e. $\gtrsim 10^{25}$ W Hz^{-1} (e.g. Giovannini et al. 2001; Giovannini 2004; Sbarrato et al. 2021).

We checked the sample of $z > 5$ sources collected from the literature for published L-band total and core flux densities and monochromatic radio powers. We used the flux densities to calculate the total (P_{total}) and core (P_{core}) K-corrected monochromatic radio powers (see Eq. 2) in cases where these values were not available. We assumed $\alpha = 0$ for calculating all P_{total} values, and those P_{core} values where α was not published. The collected parameters are listed in Table A.1 along with their references.

The top panel of Fig. 5 shows the comparison of P_{total} and P_{core} for $z > 5$ sources, where both values were available. The dashed line indicates $P_{\mathrm{total}} = P_{\mathrm{core}}$. Sources lying above this line have more extended emission, since the total power is higher than the core power. The sources become more core-dominated and more likely to be beamed as the distance from the line decreases. The sources scattering close to the $P_{\mathrm{total}} = P_{\mathrm{core}}$ line or slightly below, like some of our sources, can also be affected by variability. The colouring in the top panel of Fig. 5 reveals that in general the higher the radio loudness the less core-dominated the source appears. This implies that the radio emission responsible for the high radio loudness tends to originate from the kiloparsec-scale radio structure rather than the compact parsec-scale region.

We found that our sources, although appearing core-dominated, do not show evidence for relativistically beamed radio jets based on the derived brightness temperatures (Table 3). One reason could be that the T_{b} values are underestimated, by slightly overestimating the modelled size of the VLBI core component. However, this cannot be responsible for the nearly 2 orders of magnitude difference from the equipartition brightness temperature. A possible physical explanation is that the radio emission region of these sources is intrinsically small, confined to sub-kiloparsec scales. Gigahertz-peaked spectrum (GPS) radio sources and compact symmetric objects (CSOs) (e.g. Wilkinson et al. 1994; An & Baan 2012; O'Dea & Saikia 2021) are known to be young jetted AGN with compact radio structure, without beamed radio jets and diffuse extended emission. In fact, a few known CSOs can be found among high-redshift sources (e.g. Frey et al. 2008; Momjian et al. 2008; An et al. 2022; Krezinger et al. 2022). The GPS and CSO nature of the sources could be supported by their peaked spectrum (e.g. Tremblay et al. 2016). In our sample, only four of the sources have peaked spectra (Fig. 3), but except for J2239+0030, all the others have poor low-frequency coverage in their flux density measurements, retaining the possibility that their spectrum is actually peaked.

The middle panels of Fig. 5 display the relation between the radio-loudness indices and the derived radio powers, similar to the $T_{\mathrm{b}} - R$ plot in Sect. 5.6. Both the P_{total} and P_{core} values show a steadily increasing trend. Since R is proportional to the 5-GHz total radio power, this trend is not surprising for P_{total}. The bottom panels of Fig. 5 show the P_{total} and P_{core} values for AGN at $z > 5$ as a function of redshift. Median values for both the collected P_{total} and P_{core} are around 2×10^{26} W Hz^{-1}.

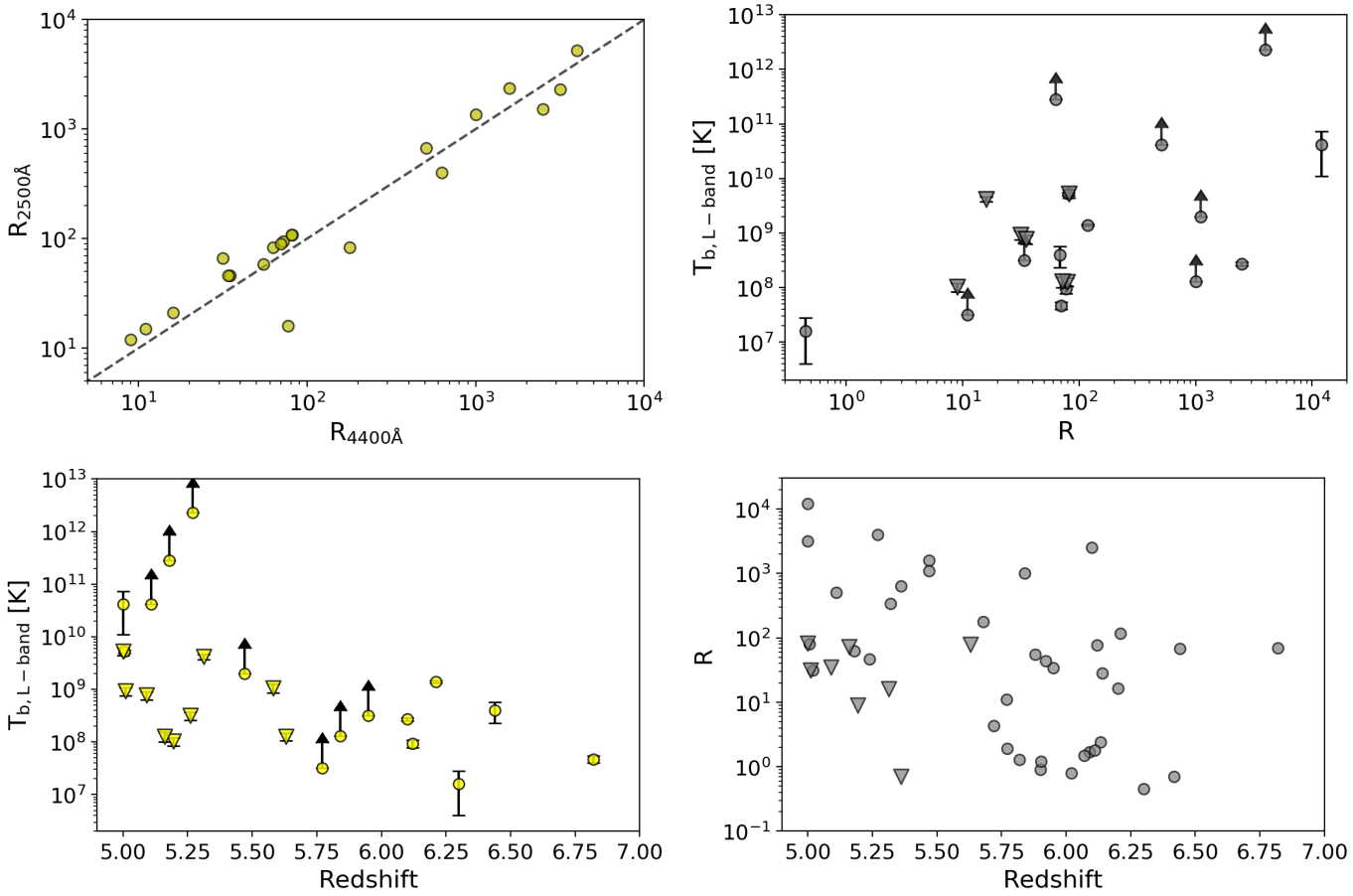

Fig. 4: Radio-loudness and brightness temperature relation of high redshift radio sources. *Top left:* The $R_{2500\,\text{Å}}$ index as a function of $R_{4400\,\text{Å}}$ for sources where both values are available in the literature. The dashed line represents $R_{2500\,\text{Å}} = R_{4400\,\text{Å}}$. *Top right:* The redshift-corrected L-band brightness temperatures as a function of radio loudness. The sources presented in this paper are marked with triangles. *Bottom left:* The redshift-corrected L-band brightness temperature measurements for all $z > 5$ AGN published to date, including those presented in this paper (triangles), as a function of redshift. *Bottom right:* The $R_{4400\,\text{Å}} = L_{5\,\text{GHz}}/L_{4400\,\text{Å}}$ and $R_{2500\,\text{Å}} = L_{5\,\text{GHz}}/L_{2500\,\text{Å}}$ (where $R_{4400\,\text{Å}}$ is not available) radio-loudness indices of $z > 5$ sources as a function of redshift.

6. Conclusion

In this paper, we present the results of 1.7-GHz VLBI observation of ten high-redshift ($5 < z < 6$) radio quasars using the EVN and e-MERLIN arrays. The sources have different radio-loudness indices spanning a wide range of $\sim 10^{-1} - 10^{2}$. Out of the ten sources, nine have been successfully detected. They all show a single faint but compact milliarcsecond-scale radio core component. The 90% detection rate for this faint sample is impressive and demonstrates the effectiveness of the observing strategy and the sensitivity of the VLBI network used. This opens the way for future VLBI studies of many more similar $z > 5$ sources. Further improvements in VLBI sensitivity expected in the future from e.g. the first phase of the Square Kilometre Array (Paragi et al. 2015) or the Five-hundred-meter Aperture Spherical Radio Telescope core array (Jiang et al. 2024) are promising for advancing this work.

The sample presented here increases the number of known VLBI-observed $z > 5$ radio AGN by about 40%. These high-resolution interferometric observations, combined with additional low-resolution radio data obtained from the literature, helped derive properties such as the origin of the radio emission, compactness, flux density variability, and spectral indices. The brightness temperatures obtained confirm the AGN origin of the radio emission and suggest that the emission in none of these sources is Doppler-enhanced. The derived monochromatic powers are comparable to those of the luminous FRII radio galaxies and quasars. As J0306+1853 remained undetected at milliarcsecond-scale, we have not been able to reveal the compact jet expected by Sbarrato et al. (2021). We found that five of the sources have *Gaia* optical astrometric positions. One of them is J0306+1853 with no VLBI detection, but the optical positions of the other four AGN were found to be consistent with the VLBI radio core positions within the uncertainties.

Notably, we did not find crucial differences in the morphology and the derived physical parameters between our detected three RQQ and six RLQ sources. These sources appear core-dominated with high radio power, despite being in the transition region of RQQs to RLQs. With no compelling evidence for Doppler-boosted jet emission, it is possible that these are young jetted AGN whose radio emission is confined to a small region around the central SMBH.

By examining this sample, supplemented with other $z > 5$ sources detected with VLBI at L-band from the literature, we found that the core brightness temperatures and monochromatic radio powers tend to increase with increasing radio loudness. However, for the $R - T_{\text{b}}$ relation, the radio-quiet and the extreme radio-loud regimes are still undersampled. High-

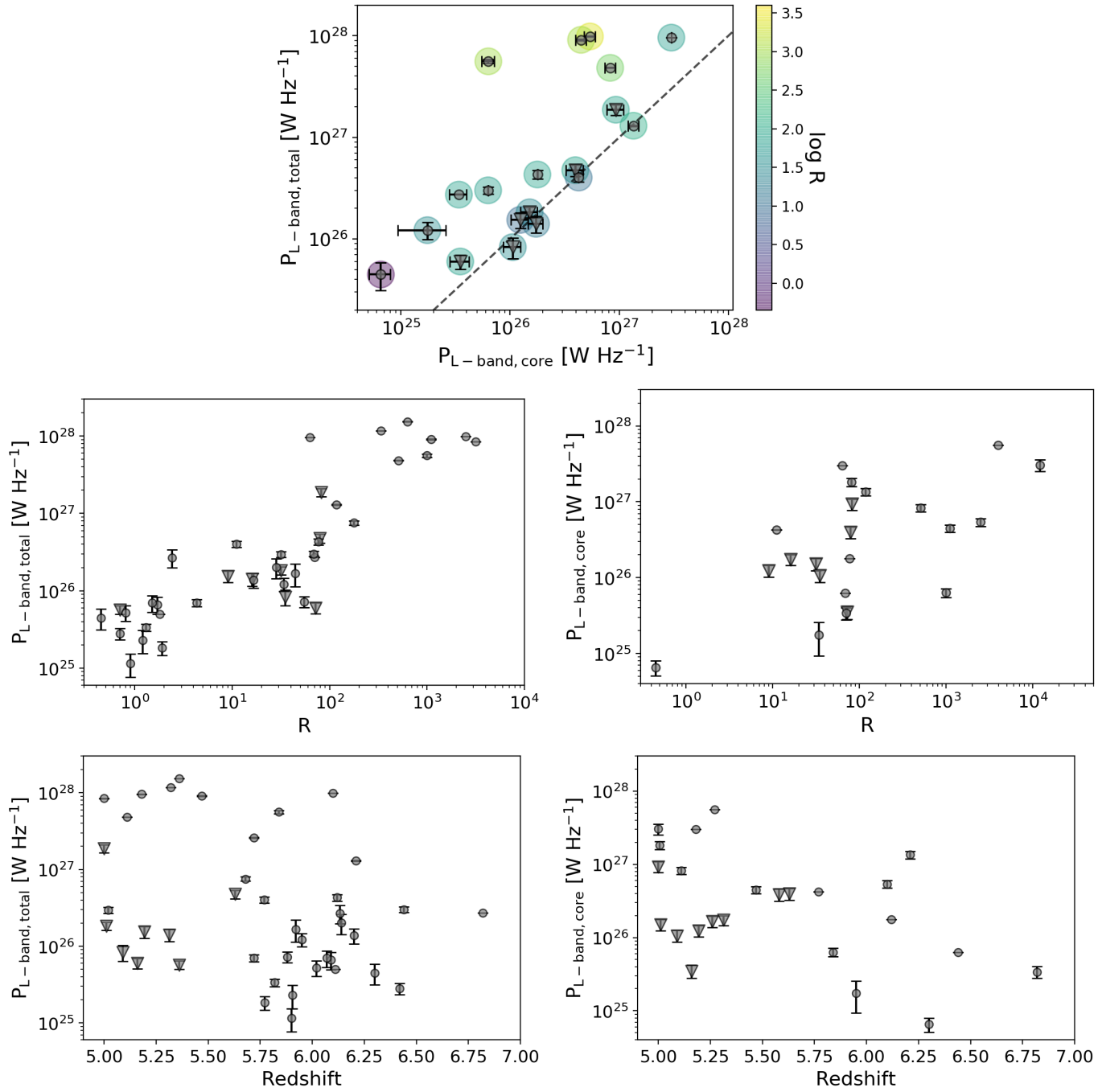

Fig. 5: L-band total and core monochromatic radio powers of high redshift radio sources. The sources presented in this paper are marked with triangles. *Top:* The comparison of L-band core monochromatic radio power and the L-band total monochromatic radio power for $z > 5$ sources where both values are available. The dashed line represents the $P_{\rm total} = P_{\rm core}$. The colours indicate the source radio loudness. *Middle:* The total *(left)* and core *(right)* monochromatic radio powers of $z > 5$ sources as a function of radio loudness. *Bottom:* The total *(left)* and core *(right)* monochromatic radio powers as a function of redshift.

resolution VLBI observations of many more radio-emitting AGN at $z > 5$ would be desirable, even though it is challenging because the spectral turnover is shifting to lower frequencies as z increases. Sensitive higher-frequency and therefore higher-resolution VLBI observations of the investigated nine detected sources would provide tighter constraints on the brightness temperature, and information on the spectral properties of the cores.

Acknowledgements. The EVN is a joint facility of independent European, African, Asian and North American radio astronomy institutes. Scientific results from data presented in this publication are derived from the following EVN project code: EG102. The e-MERLIN is a National Facility operated by the University of Manchester at Jodrell Bank Observatory on behalf of STFC. This work presents results from the European Space Agency (ESA) space mission *Gaia*. *Gaia* data are being processed by the *Gaia* Data Processing and Analysis Consortium (DPAC). Funding for the DPAC is provided by national institutions, in particular the institutions participating in the *Gaia* MultiLateral Agreement (MLA). The *Gaia* mission website is `https://www.cosmos.esa.int/gaia`. The *Gaia* archive website is `https://archives.esac.esa.int/gaia`. This research has made use of the NASA/IPAC Extragalactic Database (NED) which is operated by the Jet Propulsion Laboratory, California Institute of Technology,

under contract with the National Aeronautics and Space Administration. M.K. thanks for the support from the ÚNKP-23-3 New National Excellence Program of the Ministry for Culture and Innovation from the source of the National Research, Development and Innovation Fund. We thank the Hungarian National Research, Development and Innovation Office (NKFIH, grant no. OTKA K134213) for support. This work was also supported by HUN-REN and the NKFIH excellence grant TKP2021-NKTA-64. T.A. thanks for the support from the National SKA Program of China (2022SKA0120102).

References

An, T. & Baan, W. A. 2012, ApJ, 760, 77
An, T., Wang, A., Liu, Y., et al. 2023, MNRAS, 519, 4047
An, T., Wang, A., Zhang, Y., et al. 2022, MNRAS, 511, 4572
An, T., Wu, F., Yang, J., et al. 2012, ApJS, 198, 5
Bañados, E., Mazzucchelli, C., Momjian, E., et al. 2021, ApJ, 909, 80
Bañados, E., Venemans, B. P., Decarli, R., et al. 2016, ApJS, 227, 11
Bañados, E., Venemans, B. P., Morganson, E., et al. 2015, ApJ, 804, 118
Baldi, R. D., Williams, D. R. A., McHardy, I. M., et al. 2018, MNRAS, 476, 3478
Baldi, R. D., Williams, D. R. A., McHardy, I. M., et al. 2021, MNRAS, 500, 4749
Beasley, A. J. & Conway, J. E. 1995, in Astronomical Society of the Pacific Conference Series, Vol. 82, Very Long Baseline Interferometry and the VLBA, ed. J. A. Zensus, P. J. Diamond, & P. J. Napier, 327
Begelman, M. C., Blandford, R. D., & Rees, M. J. 1984, Reviews of Modern Physics, 56, 255
Belladitta, S., Moretti, A., Caccianiga, A., et al. 2023, A&A, 669, A134
Belladitta, S., Moretti, A., Caccianiga, A., et al. 2019, A&A, 629, A68
Belladitta, S., Moretti, A., Caccianiga, A., et al. 2020, A&A, 635, L7
Blandford, R., Meier, D., & Readhead, A. 2019, ARA&A, 57, 467
Blundell, K. M. & Beasley, A. J. 1998, MNRAS, 299, 165
Caccianiga, A., Ighina, L., Moretti, A., et al. 2024, A&A, 684, A98
Cao, H. M., Frey, S., Gabányi, K. É., et al. 2017, MNRAS, 467, 950
Cao, H. M., Frey, S., Gurvits, L. I., et al. 2014, A&A, 563, A111
Charlot, P., Jacobs, C. S., Gordon, D., et al. 2020, A&A, 644, A159
Condon, J. J. 1992, ARA&A, 30, 575
Condon, J. J., Condon, M. A., Gisler, G., & Puschell, J. J. 1982, ApJ, 252, 102
Condon, J. J., Cotton, W. D., Greisen, E. W., et al. 1998, AJ, 115, 1693
Coppejans, R., Frey, S., Cseh, D., et al. 2016, MNRAS, 463, 3260
Coppejans, R., van Velzen, S., Intema, H. T., et al. 2017, MNRAS, 467, 2039
De Rosa, G., Decarli, R., Walter, F., et al. 2011, ApJ, 739, 56
DESI Collaboration, Adame, A. G., Aguilar, J., et al. 2024, AJ, 168, 58
Diamond, P. J. 1995, in Astronomical Society of the Pacific Conference Series, Vol. 82, Very Long Baseline Interferometry and the VLBA, ed. J. A. Zensus, P. J. Diamond, & P. J. Napier, 227
Fan, X., Strauss, M. A., Schneider, D. P., et al. 1999, AJ, 118, 1
Fanaroff, B. L. & Riley, J. M. 1974, MNRAS, 167, 31P
Fey, A. L., Eubanks, M., & Kingham, K. A. 1997, AJ, 114, 2284
Fomalont, E. B. 1999, in Astronomical Society of the Pacific Conference Series, Vol. 180, Synthesis Imaging in Radio Astronomy II, ed. G. B. Taylor, C. L. Carilli, & R. A. Perley, 301
Frey, S., Gurvits, L. I., Paragi, Z., & É. Gabányi, K. 2008, A&A, 484, L39
Frey, S., Mosoni, L., Paragi, Z., & Gurvits, L. I. 2003, MNRAS, 343, L20
Frey, S., Paragi, Z., Fogasy, J. O., & Gurvits, L. I. 2015, MNRAS, 446, 2921
Frey, S., Paragi, Z., Gurvits, L. I., Cseh, D., & Gabányi, K. É. 2010, A&A, 524, A83
Frey, S., Paragi, Z., Gurvits, L. I., Gabányi, K. É., & Cseh, D. 2011, A&A, 531, L5
Gabányi, K. É., Belladitta, S., Frey, S., et al. 2023, PASA, 40, e004
Gabanyi, K. E., Cseh, D., Frey, S., et al. 2015, MNRAS, 450, L57
Gabányi, K. É., Frey, S., Gurvits, L. I., Paragi, Z., & Perger, K. 2018, Research Notes of the American Astronomical Society, 2, 200
Gabányi, K. É., Frey, S., Satyapal, S., Constantin, A., & Pfeifle, R. W. 2019, A&A, 630, L5
Gaia Collaboration, Prusti, T., de Bruijne, J. H. J., et al. 2016, A&A, 595, A1
Gaia Collaboration, Vallenari, A., Brown, A. G. A., et al. 2023, A&A, 674, A1
Ghisellini, G., Haardt, F., Ciardi, B., et al. 2015a, MNRAS, 452, 3457
Ghisellini, G., Haardt, F., Della Ceca, R., Volonteri, M., & Sbarrato, T. 2013, MNRAS, 432, 2818
Ghisellini, G. & Sbarrato, T. 2016, MNRAS, 461, L21
Ghisellini, G., Tagliaferri, G., Sbarrato, T., & Gehrels, N. 2015b, MNRAS, 450, L34
Giovannini, G. 2004, Ap&SS, 293, 1
Giovannini, G., Cotton, W. D., Feretti, L., Lara, L., & Venturi, T. 2001, ApJ, 552, 508
Giroletti, M. & Panessa, F. 2009, ApJ, 706, L260
Gordon, Y. A., Boyce, M. M., O'Dea, C. P., et al. 2020, Research Notes of the American Astronomical Society, 4, 175
Gordon, Y. A., Boyce, M. M., O'Dea, C. P., et al. 2021, ApJS, 255, 30
Greisen, E. W. 2003, in Astrophysics and Space Science Library, Vol. 285, Information Handling in Astronomy - Historical Vistas, ed. A. Heck, 109
Herrera Ruiz, N., Middelberg, E., Norris, R. P., & Maini, A. 2016, A&A, 589, L2
Heywood, I., Jarvis, M. J., Baker, A. J., et al. 2016, MNRAS, 460, 4433
Hodge, J. A., Becker, R. H., White, R. L., Richards, G. T., & Zeimann, G. R. 2011, AJ, 142, 3
Högbom, J. A. 1974, A&AS, 15, 417
Hogg, D. W., Baldry, I. K., Blanton, M. R., & Eisenstein, D. J. 2002, arXiv e-prints, astro
Ighina, L., Belladitta, S., Caccianiga, A., et al. 2021, A&A, 647, L11
Inayoshi, K., Visbal, E., & Haiman, Z. 2020, ARA&A, 58, 27
Ivezić, Ž., Menou, K., Knapp, G. R., et al. 2002, AJ, 124, 2364
Jiang, L., McGreer, I. D., Fan, X., et al. 2016, ApJ, 833, 222
Jiang, P., Chen, R., Gan, H., et al. 2024, Astronomical Techniques and Instruments, 1, 84
Keimpema, A., Kettenis, M. M., Pogrebenko, S. V., et al. 2015, Experimental Astronomy, 39, 259
Keller, P. M., Thyagarajan, N., Kumar, A., Kanekar, N., & Bernardi, G. 2024, MNRAS, 528, 5692
Kellermann, K. I., Condon, J. J., Kimball, A. E., Perley, R. A., & Ivezić, Ž. 2016, ApJ, 831, 168
Kellermann, K. I., Sramek, R., Schmidt, M., Shaffer, D. B., & Green, R. 1989, AJ, 98, 1195
Kewley, L. J., Heisler, C. A., Dopita, M. A., et al. 2000, ApJ, 530, 704
Klöckner, H. R., Martínez-Sansigre, A., Rawlings, S., & Garrett, M. A. 2009, MNRAS, 398, 176
Kovalev, Y. Y., Kellermann, K. I., Lister, M. L., et al. 2005, AJ, 130, 2473
Kovalev, Y. Y., Petrov, L., & Plavin, A. V. 2017, A&A, 598, L1
Krezinger, M., Frey, S., Paragi, Z., & Deane, R. 2020, Symmetry, 12, 527
Krezinger, M., Perger, K., Gabányi, K. É., et al. 2022, ApJS, 260, 49
Lacy, M., Baum, S. A., Chandler, C. J., et al. 2020, PASP, 132, 035001
Lambert, S., Sol, H., & Pierron, A. 2024, A&A, 684, A202
Lee, S.-S., Lobanov, A. P., Krichbaum, T. P., et al. 2008, AJ, 136, 159
Liu, Y., An, T., Guo, S., et al. 2024, A&A, 685, A111
Liu, Y., Wang, R., Momjian, E., et al. 2021, ApJ, 908, 124
Liu, Y., Wang, R., Momjian, E., et al. 2022, ApJ, 929, 69
Martí-Vidal, I., Ros, E., Pérez-Torres, M. A., et al. 2010, A&A, 515, A53
McGreer, I. D., Helfand, D. J., & White, R. L. 2009, AJ, 138, 1925
Middelberg, E., Deller, A., Morgan, J., et al. 2011, A&A, 526, A74
Middelberg, E., Roy, A. L., Nagar, N. M., et al. 2004, A&A, 417, 925
Momjian, E., Bañados, E., Carilli, C. L., Walter, F., & Mazzucchelli, C. 2021, AJ, 161, 207
Momjian, E., Carilli, C. L., Bañados, E., Walter, F., & Venemans, B. P. 2018, ApJ, 861, 86
Momjian, E., Carilli, C. L., & McGreer, I. D. 2008, AJ, 136, 344
Mosoni, L., Frey, S., Gurvits, L. I., et al. 2006, A&A, 445, 413
O'Dea, C. P. & Saikia, D. J. 2021, A&A Rev., 29, 3
Onken, C. A., Wolf, C., Bian, F., et al. 2022, MNRAS, 511, 572
Padovani, P., Bonzini, M., Kellermann, K. I., et al. 2015, MNRAS, 452, 1263
Panessa, F., Baldi, R. D., Laor, A., et al. 2019, Nature Astronomy, 3, 387
Panessa, F. & Giroletti, M. 2013, MNRAS, 432, 1138
Paragi, Z., Godfrey, L., Reynolds, C., et al. 2015, in Advancing Astrophysics with the Square Kilometre Array (AASKA14), 143
Pearson, T. J. 1995, in Astronomical Society of the Pacific Conference Series, Vol. 82, Very Long Baseline Interferometry and the VLBA, ed. J. A. Zensus, P. J. Diamond, & P. J. Napier, 267
Pearson, T. J. & Readhead, A. C. S. 1984, ARA&A, 22, 97
Peterson, B. M. 2006, in Physics of Active Galactic Nuclei at all Scales, ed. D. Alloin, Vol. 693, 77
Petrov, L., Kovalev, Y. Y., & Plavin, A. V. 2019, MNRAS, 482, 3023
Plavin, A. V., Kovalev, Y. Y., & Petrov, L. Y. 2019, ApJ, 871, 143
Porcas, R. W. 2009, A&A, 505, L1
Readhead, A. C. S. 1994, ApJ, 426, 51
Ross, N. P. & Cross, N. J. G. 2020, MNRAS, 494, 789
Sbarrato, T. 2021, Galaxies, 9, 23
Sbarrato, T., Ghisellini, G., Giovannini, G., & Giroletti, M. 2021, A&A, 655, A95
Sbarrato, T., Ghisellini, G., Nardini, M., et al. 2012, MNRAS, 426, L91
Sbarrato, T., Ghisellini, G., Tagliaferri, G., et al. 2015, MNRAS, 446, 2483
Sbarrato, T., Ghisellini, G., Tagliaferri, G., et al. 2022, A&A, 663, A147
Schwab, F. R. & Cotton, W. D. 1983, AJ, 88, 688
Shao, Y., Wagg, J., Wang, R., et al. 2020, A&A, 641, A85
Shao, Y., Wagg, J., Wang, R., et al. 2022, A&A, 659, A159
Shen, Y., Wu, J., Jiang, L., et al. 2019, ApJ, 873, 35
Shepherd, M. C., Pearson, T. J., & Taylor, G. B. 1994, in Bulletin of the American Astronomical Society, Vol. 26, 987–989

Sokolovsky, K. V., Kovalev, Y. Y., Pushkarev, A. B., & Lobanov, A. P. 2011, A&A, 532, A38
Sotnikova, Y., Mikhailov, A., Mufakharov, T., et al. 2024, Galaxies, 12, 25
Sotnikova, Y., Mikhailov, A., Mufakharov, T., et al. 2021, MNRAS, 508, 2798
Spingola, C., Dallacasa, D., Belladitta, S., et al. 2020, A&A, 643, L12
Sramek, R. A. & Weedman, D. W. 1980, ApJ, 238, 435
Tremblay, S. E., Taylor, G. B., Ortiz, A. A., et al. 2016, MNRAS, 459, 820
Ulvestad, J. S., Antonucci, R. R. J., & Barvainis, R. 2005, ApJ, 621, 123
Volonteri, M. 2012, Science, 337, 544
Volonteri, M., Haardt, F., Ghisellini, G., & Della Ceca, R. 2011, MNRAS, 416, 216
Wang, A., An, T., Cheng, X., et al. 2023a, MNRAS, 518, 39
Wang, A., An, T., Zhang, Y., et al. 2023b, MNRAS, 525, 6064
Wang, F., Wu, X.-B., Fan, X., et al. 2015, ApJ, 807, L9
Wang, F., Wu, X.-B., Fan, X., et al. 2016, ApJ, 819, 24
Wang, F., Yang, J., Fan, X., et al. 2019, ApJ, 884, 30
Wang, R., Wagg, J., Carilli, C. L., et al. 2013, ApJ, 773, 44
White, R. L., Becker, R. H., Helfand, D. J., & Gregg, M. D. 1997, ApJ, 475, 479
Wilkinson, P. N., Polatidis, A. G., Readhead, A. C. S., Xu, W., & Pearson, T. J. 1994, ApJ, 432, L87
Wright, E. L. 2006, PASP, 118, 1711
Wu, X.-B., Wang, F., Fan, X., et al. 2015, Nature, 518, 512
Yang, J., Wang, F., Fan, X., et al. 2019, ApJ, 871, 199
Yang, J., Wang, F., Wu, X.-B., et al. 2016, ApJ, 829, 33
Yue, M., Fan, X., Yang, J., & Wang, F. 2023, AJ, 165, 191
Zhang, Y., An, T., Wang, A., et al. 2022, A&A, 662, L2

Appendix A: Radio loudness and brightness temperatures

Table A.1: Values and references for the collected radio-loudness indices, L-band brightness temperatures, core flux densities, monochromatic powers, and black hole masses for the $z > 5$ radio AGN listed with increasing redshift.

Redshift	Source ID	$R_{4400\,\text{Å}}$	Ref.	$R_{2500\,\text{Å}}$	Ref.	$T_{\text{b,L-band}}$ [10^8 K]	Ref.	$S_{\text{total,L-band}}$ [mJy]	Ref.	$S_{\text{core,L-band}}$ [mJy]	Ref.	$P_{\text{total,L-band}}$ [10^{26} W Hz^{-1}]	Ref.	$P_{\text{core,L-band}}$ [10^26 W Hz^{-1}]	Ref.	M_{SMBH} $10^8 M_\odot$	Ref.
5.00	J2344+1653	82	32	108	32	53.0 (8.9)	0			7.0 (0.9)	0	18.7 (2.3)	0	9.3 (1.6)	0		
5.00	J0141−5427			12000	5	420 (310)	18	160	5	80.3 (8.4)	18	419	0	30.4 (5.3)	0	8	5
5.00	GB6J162956+095959	3162	8	2300	5			32.3 (0.1)	35			84.4 (0.3)	0				
5.01	J1146+4037	81	4	108	4	52.1 (2.9)	14			15.5 (0.8)	14			18.3 (2.3)	14		
5.01	J1034+2033	32	8	66	4	9.2 (1.6)	0	3.9 (0.1)	35	3.5 (0.5)	0	1.8 (0.2)	0	1.5 (0.3)	0		
5.02	J1013+3518	32	8					1.1 (0.1)	35			3.0 (0.3)	0				
5.09	J2239+0030	35	32	46	32	7.7 (1.4)	0	1.4 (0.1)	35	1.4 (0.2)	0	0.8 (0.2)	0	1.1 (0.2)	0		
5.11	J0913+5919	509	4	674	4	420	38	17.6 (0.1)	35	19.4 (0.1)	38	48.3 (0.3)	0	8.3 (0.9)	0		
5.16	J2245+0024	72	4	94	4	1.3 (0.3)	0	0.9 (0.1)	35	0.8 (0.1)	0	0.6 (0.1)	0	0.4 (0.1)	0		
5.18	J0131−0321	63	4	83	4	2800	16	33.7 (0.1)	35	64.4 (0.3)	16	95.8 (0.3)	0	30	16	110	19
5.19	J0741+2521	9	4	12	4	1.0 (0.2)	0	2.9 (0.1)	35	2.7 (0.4)	0	1.5 (0.3)	0	1.2 (0.2)	0		
5.24	J2329+3003			47	26												
5.26	J0747+1153					3.1 (0.6)	0			1.8 (0.2)	0			1.7 (0.3)	0		
5.27	J1026+2542	3981	8	5200	27	23000	15	239.4 (0.1)	35	180.4 (0.5)	15	708.9 (0.3)	0	56	15		
5.31	J1614+4640	16	4	21	4	41.7 (4.5)	0	2.2 (0.1)	35	3.6 (0.4)	0	1.4 (0.3)	0	1.7 (0.3)	0		
5.32	PSO J191+86	337	7					74.2 (2.3)	10			117	7			24	7
5.36	J0306+1853	0.7	28					0.3	28			0.6 (0.1)	0			110	36
5.36	GB6J164856+460341	631	8	400	5			49.9 (0.1)	35			153.6 (0.3)	0				
5.47	J1702+1301	1100	32			20	24	28.3 (0.4)	24	8.4 (0.1)	24	91.2 (1.3)	0	4.5 (0.5)	0		
5.47	J0906+6930	1585	8	2373	26												
5.58	J0616−1338					10.6 (2.0)	0			1.9 (0.3)	0			3.9 (0.7)	0		
5.63	J0901+1615	79.4	8			1.3 (0.2)	0	3.9 (0.1)	35	3.1 (0.4)	0	4.8 (0.6)	0	3.9 (0.7)	0		
5.68	PJ055−00	178	2	83	26			2.1 (0.1)	2			7.5 (0.5)	0				
5.72	J1530+1049							7.3 (0.1)	35	1.7	17	25.9 (0.4)	0	0.9	0		
5.72	J0203+0012	4.3	2					0.20 (0.02)	2			0.7 (0.1)	0				
5.77	0836+0054	11	4	15	4	0.3	12	1.1 (0.1)	35	1.1	12	4.0 (0.4)	0	4.3	12	83	30
5.77	J0927+2001	1.9	2					0.05 (0.01)	2			0.18 (0.04)	0			49	30
5.82	J0002+2550	1.3	2					0.09 (0.01)	2			0.34 (0.04)	0			48	30
5.84	P352−15	1000	25	1352	26	1.3	25	14.9 (0.7)	10	1.2 (0.1)	25	56.0 (2.6)		0.6 (0.1)	0		
5.88	J2242+0334	55	22	58	26			0.19 (0.03)	22			0.7 (0.1)	0				
5.90	J1335+3533	0.9	2					0.03 (0.01)	2			0.12 (0.04)	0			29	30
5.90	J1411+1217	1.2	2					0.06 (0.02)	2			0.2 (0.1)	0			5	11
5.92	J2053+0047	44	2					0.4 (0.1)	2			1.7 (0.5)	0				
5.95	J2228+0110	34	4	46	4	3.1	9	0.3 (0.1)	2	0.3 (0.1)	9	1.2 (0.2)	0	0.2 (0.1)	0		
6.02	J0818+1722	0.8	21					0.13 (0.03)	21			0.5 (0.1)	0				
6.07	J1034−1425	1.5	21					0.17 (0.04)	21			0.7 (0.2)	0				
6.09	J1602+4228	1.7	21					0.16 (0.04)	21			0.7 (0.2)	0			24	30
6.10	PSO J0309+27	2500	6	1521	26	2.7 (0.2)	31	23.7 (0.1)	10	8.0 (0.1)	31	98.5		5.4 (0.6)	0		
6.11	J1558−0724	1.8	21					0.12 (0.04)	21			0.5	0				
6.12	J1427 +3312	77	21	16	4	0.9 (0.2)	13	1.0 (0.1)	35	1.5	13	4.3 (0.4)	0	1.8	13	11	30
6.13	J1319+0950	2.4	2					0.6 (0.2)	22			2.7 (0.7)	0			21	34
6.14	J1609+3041	28.3	2					0.5 (0.1)	2			2.0 (0.6)	0			43	30
6.20	J0227−0605	16.5	22					0.3 (0.1)	22			1.4 (0.3)	0			2	30
6.21	J1429+5447	118	21			14.0 (0.6)	37	3.00 (0.04)	21	3.3 (0.1)	37	12.9 (0.2)	0	13.5 (1.5)	37	18	30
6.30	J0100+2802	0.5	28			0.2 (0.1)	23	0.10 (0.03)	21	0.09 (0.02)	23	0.5 (0.1)	0	0.07 (0.01)	0	120	36
6.42	J1148+5251	0.7	2					0.06 (0.01)	2			0.3 (0.1)	0			87	30
6.44	VIK J2318−3113	69	21			4.0 (1.7)	33	0.6 (0.1)	21	0.6 (0.1)	33	3.0 (0.2)	0	0.63	33	6	20
6.82	P172+18	70	26	90	26	0.5 (0.1)	26	0.5	3	0.4 (0.1)	26	2.7	0	0.3 (0.1)	0		

Notes. Col. 1 – source redshift; Col. 2 – source designation; Col. 3-4 – $R_{4400\,\text{Å}} = L_{5\,\text{GHz}}/L_{4400\,\text{Å}}$ radio-loudness index and reference number; Col. 5-6 – $R_{2500\,\text{Å}} = L_{5\,\text{GHz}}/L_{2500\,\text{Å}}$ radio-loudness index and reference number; Col. 7-8 – L-band core brightness temperature (with uncertainty in parentheses) and reference number; Col. 9-10 – L-band total flux density (with uncertainty in parentheses) and reference number; Col. 11-12 – L-band core flux density (with uncertainty in parentheses) and reference number; Col. 13-14 – L-band total radio power (with uncertainty in parentheses) and reference number; Col. 15-16 – L-band core radio power (with uncertainty in parentheses) and reference number; Col. 17-18 – estimated black hole mass and reference number. The literature references are the following. 0: This paper; 1:An et al. (2023); 2: Bañados et al. (2015); 3: Bañados et al. (2021); 4: Shao et al. (2022); 5: Belladitta et al. (2019); 6: Belladitta et al. (2020); 7: Belladitta et al. (2023); 8: Caccianiga et al. (2024); 9: Cao et al. (2014); 10: Condon et al. (1998); 11: De Rosa et al. (2011); 12: Frey et al. (2003); 13: Frey et al. (2008); 14: Frey et al. (2010); 15: Frey et al. (2015); 16: Gabanyi et al. (2015); 17: Gabányi et al. (2018); 18: Gabányi et al. (2023); 19: Ghisellini et al. (2015b); 20: Ighina et al. (2021); 21: Keller et al. (2024); 22: Liu et al. (2021); 23: Liu et al. (2022); 24: Liu et al. (2024); 25: Momjian et al. (2018); 26: Momjian et al. (2021); 27: Sbarrato et al. (2012); 28: Sbarrato et al. (2021); 29: Shao et al. (2022); 30: Shen et al. (2019); 31: Spingola et al. (2020); 32: Yang et al. (2016); 33: Zhang et al. (2022); 34: Wang et al. (2013); 35: White et al. (1997); 36: Wu et al. (2015); 37: Frey et al. (2011); 38: Coppejans et al. (2016)